Journal of Functional Materials and Applied Engineering

Research Paper

Preparation and High-Temperature Properties of Low-Cost Basalt Fiber Reinforced Aerogel Composites

Rajesh Karok[1], Peter Kemefa[2], Jacobs Sharma[2,*]

[1] Green Processing, Bioremediation and Alternative Energies Research Group, Faculty of Environment and Labour Safety, Ton Duc Thang University, Ho Chi Minh City, Viet Nam
[2] Chemical and Environmental Engineering Department, University of the Basque Country, Plaza Europa, 1, 20018 Donostia-San Sebastián, Spain
*Corresponding author: jacobssharma@ehu.es

Abstract. To address the thermal runaway risk of lithium-ion batteries in new energy vehicles, this study developed a basalt fiber reinforced aerogel composite thermal insulation pad using an atmospheric pressure drying process. Methods By regulating the concentration of tetraethyl orthosilicate (TEOS), the ambient-temperature properties of the composites were optimized, and the high-temperature performance was investigated via heating treatment and flame exposure experiments. Results TEOS molarity exerted substantial influence on aerogel architectural and functional attributes. At 1.00 mol/L precursor concentration, the composite achieved superior ambient-condition performance: thermal conductivity minimized to 0.0254 W/(m • K), compressive resistance of 121 kPa, and complete elastic recovery upon load removal. Elevated-temperature behavior was equally remarkable: thermal conductivity remained merely 0.0494 W/(m • K) at 500° C; following 700° C exposure for 24 h, abundant mesoporosity was preserved; after 1090° C butane flame impingement for 20 min, sintering remained confined to a superficial 2 mm stratum.Conclusion The composite material developed in this study offers a low-cost, high-performance solution for the passive thermal protection of power batteries.

Keywords: *Basalt fiber needle-punched felt; Aerogel composite; Mechanical properties; Atmospheric pressure drying; Thermal insulation*

Received on 15 Dec 2021, Accepted on 15 Apr 2022, Published on 28 Apr 2022

1 Introduction

Lithium-ion power batteries are favored for their high energy density; however, they are susceptible to thermal runaway induced by external mechanical abuse or overcharging, leading to fire and explosion that can propagate throughout the battery pack, causing property damage and threatening lives [1]. Passive thermal protection systems represent one of the most economical, simple, and effective strategies to prevent thermal runaway and its propagation [2]. The surface temperature of mainstream ternary lithium batteries during thermal runaway can reach 700°C, posing severe challenges to the high-temperature stability of insulation materials. Conventional thermal barrier materials, exemplified by mica laminates and ceramic fiber batting, demonstrate inadequate efficacy in suppressing thermal runaway cascade propagation. Fiber-reinforced aerogel felts have emerged as a primary choice for passive thermal protection in batteries due to their non-combustibility, excellent thermal insulation [3], and compressibility [4], effectively blocking thermal propagation [5]. The superior insulation performance of these materials stems from their core component—silica aerogel. Silica aerogel possesses a three-dimensional networked nanoporous structure composed of secondary silica particles, achieving a porosity of up to 99.8% and a specific surface area of 500–1500 m^2/g, making it one of the lowest density solid materials known [6–9]. Its unique nanoporous structure confers multi-scale heat transfer suppression mechanisms: the pore size is smaller than the mean free path of air molecules, effectively blocking convective heat transfer; the porous structure significantly extends the solid heat conduction path; and the high specific surface area of the pore walls effectively inhibits infrared radiative heat transfer [10]. The synergy of these mechanisms makes it

one of the solids with the lowest thermal conductivity (ca. 0.014 W/(m·K)) [11–13].

However, silica aerogels consist of microscopic porous structures, suffering from low mechanical strength, fragility, and dusting issues, which restrict their practical application. Fiber incorporation has emerged as a viable strategy to circumvent these constraints, demonstrably enhancing mechanical integrity and operational durability [14–16]. Peng et al. [17] synthesized mullite fiber-reinforced alumina-silica aerogel composites through supercritical desiccation, which retained minimal shrinkage and thermal insulating capacity under 1500°C flame exposure. Li et al. [18] developed flexible aramid fiber-reinforced silica aerogel composites via ambient-pressure drying, attaining thermal conductivity of 0.023 W/(m·K) alongside flexural modulus of 1.42 MPa and strength of 0.18 MPa. Wu et al. [19] engineered a stratified aerogel architecture comprising silica fibers, silicon carbide nanowires, and silica aerogel matrix, achieving thermal conductivity of 0.017 W/(m·K) at 25°C, tensile capacity of 0.75 MPa, and dimensional stability following 1000°C thermal treatment for 30 min. However, current fiber-reinforced aerogel materials face challenges: organic fibers (e.g., aramid) cannot meet the thermal protection demands of high-temperature batteries; high-performance ceramic fibers (e.g., mullite, SiC) are expensive and complex to process; and while commercial glass fiber reinforced aerogel felts are low-cost, their high-temperature performance is insufficient. Conversely, basalt fiber represents an innovative inorganic reinforcement distinguished by superior tensile strength, elevated elastic modulus, thermal resilience, chemical inertness, ecological compatibility, and economic viability, thereby presenting extensive industrial applicability [20]. Therefore, adopting relatively low-cost basalt fiber as a reinforcing material is an excellent alternative. Ge et al. [21] indicated that basalt fiber felt reinforced aerogel materials prepared via supercritical drying exhibit superior high-temperature insulation performance compared to glass fiber counterparts. Notably, most existing fiber-reinforced aerogel products are prepared via supercritical drying, a technique limited by expensive equipment, high working pressure, and operational complexity [22], hindering large-scale production. In contrast, atmospheric pressure drying offers prominent advantages, including simple equipment, easy operation, good safety, and low process cost, representing a research hotspot with greater industrial potential.

To develop an insulation pad suitable for the thermal protection of new energy vehicle power batteries—combining excellent insulation performance, good mechanical properties, and cost advantages—this work utilized low-cost basalt fiber as the reinforcing material. Basalt fiber needle-punched felt reinforced aerogel composites (BF/SAC) with different TEOS concentrations were prepared via a low-cost and simple atmospheric pressure drying process. The structural characteristics and ambient-temperature properties were systematically investigated, and the sample with the best ambient performance was selected to further explore the morphology, structure, and high-temperature performance after heating treatment.

2. Experimental Section

2.1 Materials and Substrate Preparation

Basalt fiber needle-punched felt (thickness 6 mm, nominal density 100 kg/m³), Chongqing Zhiduo New Materials Technology Co., Ltd.; Tetraethyl orthosilicate (TEOS) and Hydrochloric acid (HCl), analytically pure, Sinopharm Chemical Reagent Co., Ltd.; Trimethylchlorosilane (TMCS), analytical grade, Beijing Myriad Scientific Co., Ltd.; Absolute ethanol (EtOH), analytical grade, Modern Oriental (Beijing) Technology Development Co., Ltd.; n-Hexane, analytical grade, Shanghai Titan Scientific Co., Ltd.; Ammonium hydroxide solution ($NH_3 \cdot H_2O$), analytical grade, Shanghai YiEn Chemical Technology Co., Ltd.

2.2 Material Preparation

TEOS and deionized water were mixed at molar concentration ratios x:4.5x, where x=0.67,0.83,1.00,1.17mol/L, and stirred uniformly. A hydrolysis catalyst was prepared by dissolving 30 μL concentrated hydrochloric acid in 20 mL absolute ethanol, then introducing this solution into the TEOS/deionized water blend under 15 min agitation to facilitate alkoxide hydrolysis. Concurrently, 75 μL ammonium hydroxide was diluted with absolute ethanol to a final volume of 90 mL. The ammonia-alcohol solution was added dropwise to the beaker, stirred for 5 min, and then poured into a mold containing basalt fiber needle-punched felt (6 mm). Sealed with polyethylene film, the mixture underwent gelation and aging in a 40°C water bath for 12 h. The gelled samples were demolded and transferred to ethanol for continued aging at 40°C for 12 h. Subsequently, they were immersed in 1000 mL

of n-hexane with 20 mL of TMCS for modification for 12 h. After modification, they were cleaned in n-hexane for 12 h (with solvent replacement once). After cleaning, samples were dried at 60°C for 4 h, 100°C for 3 h, and 140°C for 2 h to obtain basalt fiber needle-punched felt reinforced aerogel composites. Samples with TEOS concentrations of 0.67, 0.83, 1.00, and 1.17 mol/L were designated BF/SAC-1, BF/SAC-2, BF/SAC-3, and BF/SAC-4, respectively.

2.3 Sample Characterization

Microstructural morphology was examined via Scanning Electron Microscopy (ZEISS Crossbeam 350) following 90 s gold metallization. Thermal transport properties were quantified using a Thermal Constant Analyzer (HotDisk 2500S). Simultaneous thermogravimetric and calorimetric analysis was conducted on a NETZSCH STA 449 F3 from ambient temperature to 1000°C in oxidative atmosphere at 10 K/min heating rate. Porosity characteristics were assessed via nitrogen sorption (BELSORP Max II) after 10 h degassing at 120°C. Vibrational spectroscopy was performed on a Shimadzu IRTracer 100 in attenuated total reflectance mode (400–4000 cm^{-1}). Mechanical compression behavior was evaluated on an electromechanical universal testing frame at 2 mm/min displacement rate using 40 mm × 40 mm × 6 mm specimens. Practical service performance was evaluated by heating the bottom surface of a 100 mm × 100 mm × 6 mm composite to 600°C and measuring the temperature rise on the backside cold plate over 10 min. Flame resistance under extreme conditions was tested by exposing the sample to a butane flame for 20 min or until burnout; the nozzle was positioned 8 cm from the sample, with a flame temperature of (1090 ± 20)°C. A schematic of sample clamping and the flame test is shown in Figure 1.

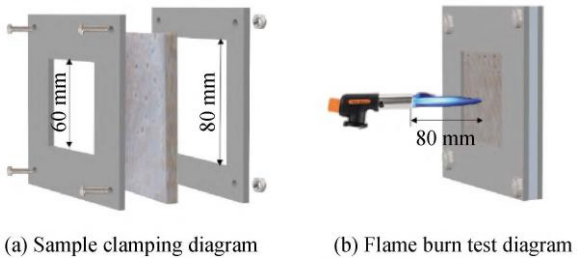

Figure 1 Schematic illustration of sample clamping and flame ignition experiment

3. Results and Discussion

3.1 Effect of TEOS Concentration on BF/SAC

3.1.1 Surface Morphology and Structure

Figure 2 shows the macro- and microscopic morphology of BF/SAC samples prepared via atmospheric drying with different TEOS concentrations. At 0.67 mol/L, the aerogel in sample BF/SAC-1 could not fully fill the gaps between fibers, appearing mostly as blocky attachments on the fiber surface with weak matrix strength. It could not withstand the capillary pressure during drying, resulting in significant shrinkage and visible cracks [23]. Increasing the TEOS concentration resulted in a more continuous and complete aerogel matrix [24], with a crack-free surface and most fibers embedded within the matrix, showing no large pores. When the TEOS concentration exceeded 0.83 mol/L, the aerogel structural strength increased, and the dried samples exhibited complete surfaces without obvious cracks.

Table 1 lists the basic physical parameters of BF/SAC with different TEOS concentrations. With TEOS molarity escalating from 0.67 to 1.17 mol/L, both the composite bulk density (ρcom) and neat aerogel density (ρaero) exhibited progressive augmentation. Specifically, ρcom rose from 0.148 to 0.182 g/cm^3, while ρaero increased from 0.062 to 0.102 g/cm^3. The porosity (ϕ_{com}), calculated by Equation (1), slightly decreased from 93.9% to 92.3%. Higher precursor concentrations led to denser SiO_2 skeletons. The sample BF/SAC-3 (TEOS 1.00 mol/L) exhibited the lowest shrinkage rate, with ρ_{com} =0.159g/cm^3 and ρ_{aero}=0.08g/cm^3, which are relatively low [25].

$$\varphi_{com} = 1 - \frac{\rho_{aero}}{\rho_S} - \frac{\rho_f}{\rho_{BF}} \quad (1)$$

Where ρ_S is the bulk density of SiO_2, taken as ρ_S=2.2g/cm³; ρBF is the density of basalt fiber, taken as ρBF =2.8g/cm³.

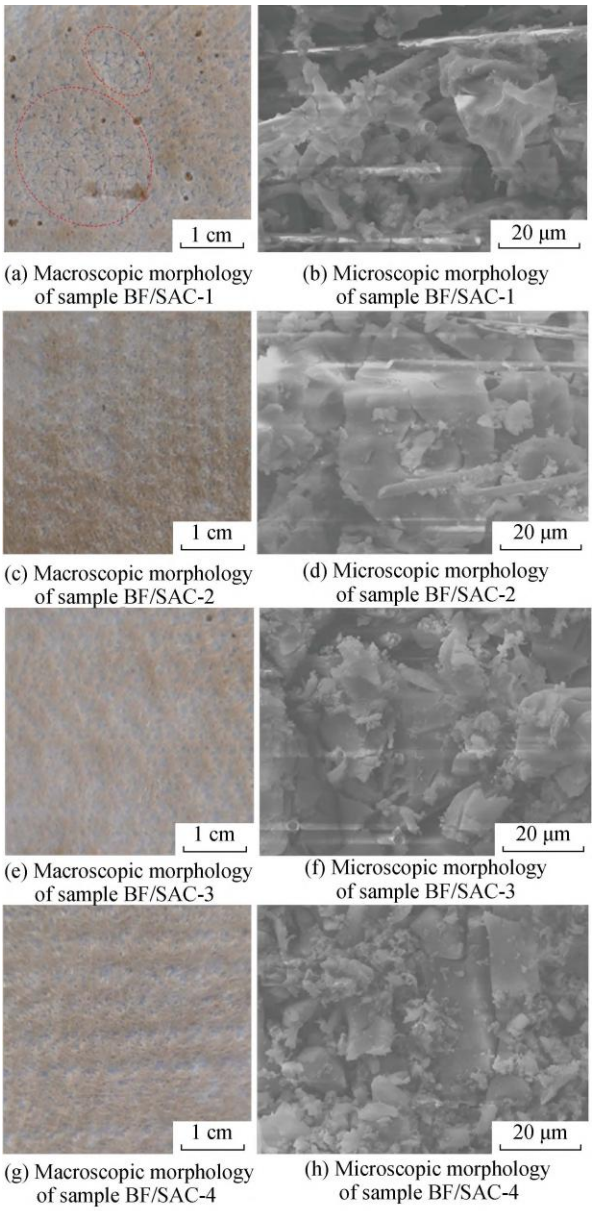

Figure 2 Morphology of BF/SAC with different TEOS concentrations

Figure 3 and Figure 4 illustrate the pore structure characteristics of BF/SAC with different TEOS concentrations. Per IUPAC nomenclature, the BF/SAC sorption isotherms conform to Type IV classification with H3 hysteresis profiles, characteristic of agglomerated particle assemblies possessing extensive mesoporosity and elevated specific surface area [26]. The BET specific surface area increased with TEOS concentration, reaching a maximum of 465.7 m²/g. The average pore size and pore volume decreased with increasing TEOS concentration, suggesting

that higher concentrations improved the retention of fine pores during drying, shifting the average pore size toward smaller diameters.

Table 1 Basic parameters of BF/SAC with different TEOS concentrations

CTEOS/ (mol·L^{-1})	ρcom/ (g·cm^{-3})	ρaero/ (g·cm^{-3})	ρg/ (g·cm^{-3})	Shrinkage / %	ϕcom/ %
0.67	0.148	0.062	0.091	56.2	93.9
0.83	0.168	0.083	0.090	66.1	93.0
1.00	0.159	0.080	0.085	33.3	93.3
1.17	0.182	0.102	0.087	45.7	92.3

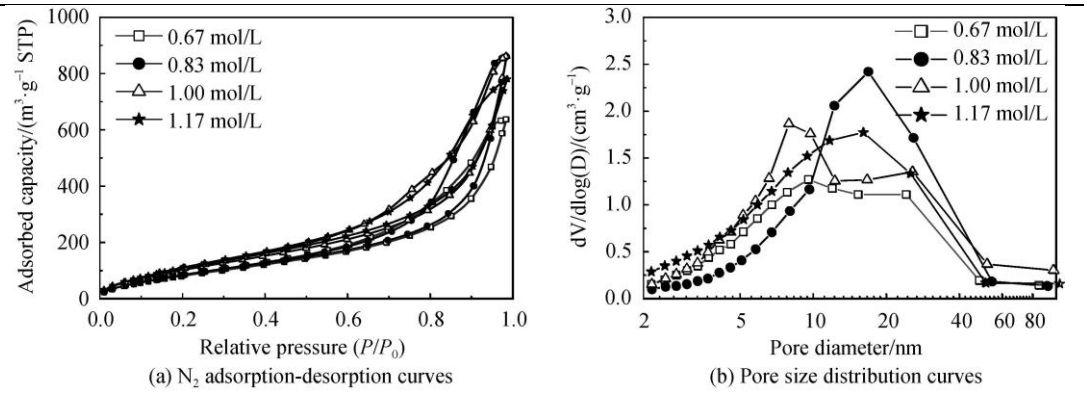

Figure 3 N2 adsorption–desorption curves and pore size distribution curves of BF/SAC with different TEOS concentrations

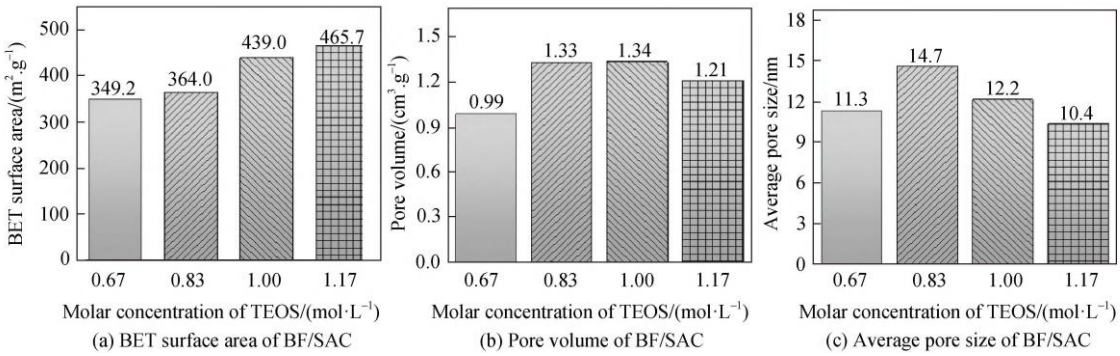

Figure 4 Pore parameters of BF/SAC with different TEOS concentrations

3.1.2 Ambient-Temperature Insulation and Mechanical Properties

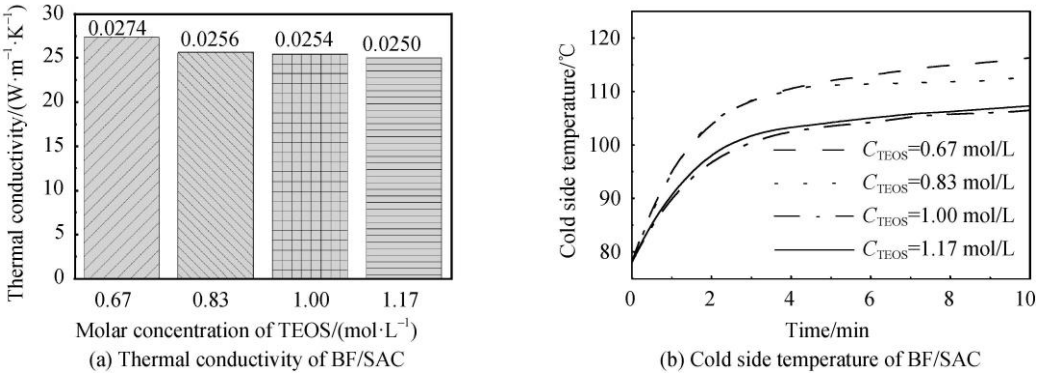

Figure 5 Thermal conductivity and cold side temperature of BF/SAC with different TEOS concentrations

Figure 5 shows the thermal conductivity and cold-side temperature of BF/SAC samples with different TEOS concentrations. At 0.67 mol/L, the aerogel failed to fill the fiber interstices, resulting in large pores within the sample. These pore dimensions surpassed the molecular mean free path of air (69 nm), consequently elevating thermal conductivity to 0.0274 W/(m·K). As TEOS concentration increased, the aerogel matrix became complete and non-fragmented, and the samples were dominated by mesoporous structures, which significantly blocked gas convection and reduced thermal conductivity. Nevertheless, pore architectural refinement remained constrained; although specific surface area expanded, mean pore diameter contracted [27]. Additionally, elevated bulk density augmented solid-phase thermal transport, maintaining BF/SAC thermal conductivity near 0.0250 W/(m·K).

Figure 5b shows that all samples possessed good insulation effects, with cold-side temperatures below 120°C. Samples BF/SAC-3 and BF/SAC-4 exhibited the lowest cold-side temperatures; after heating the hot side to 600°C for 10 min, the center temperature stabilized around 106°C, consistent with thermal conductivity results, demonstrating excellent insulation performance [28].

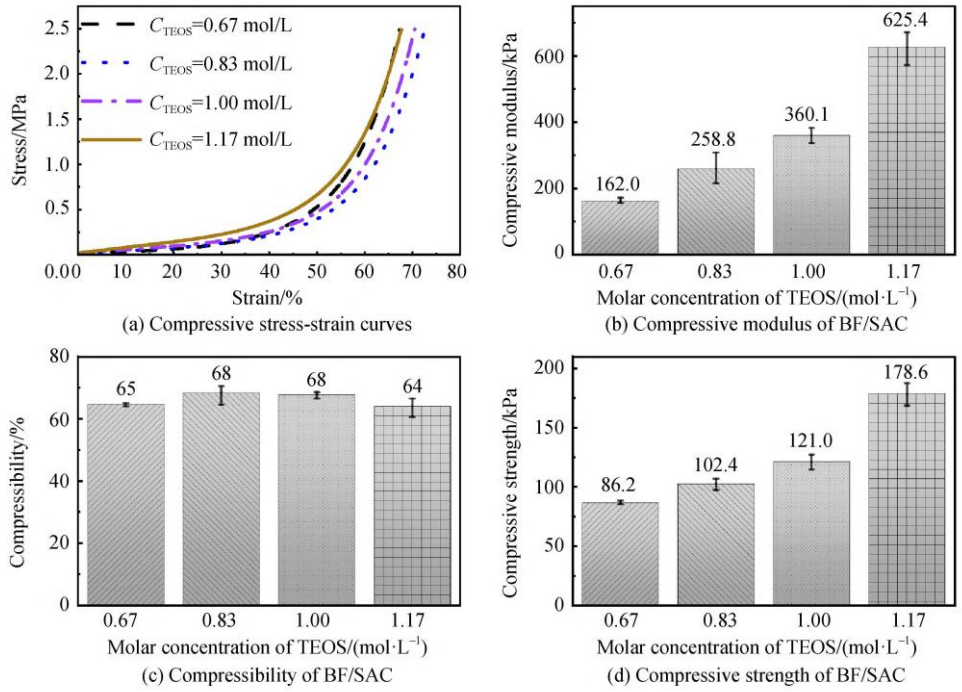

Figure 6 Compressive properties of BF/SAC with different TEOS concentrations

Figure 6 shows the compression properties of BF/SAC samples prepared via atmospheric drying. The compressive stress-strain curves exhibit three-stage characteristics: elastic compression, densification, and compaction [29]. As TEOS concentration increased, the pore wall structural strength of the aerogel increased, leading to higher compressive modulus and strength. Sample BF/SAC-4 showed the highest values: 625.4 kPa and 178.6 kPa, respectively. The basalt fiber needle-punched felt primarily bore the load, resulting in no significant difference in compression rates among samples. The high compression ratio of BF/SAC indicates good cushioning and energy absorption.

3.2 Effect of Heating on Sample BF/SAC-3

3.2.1 Surface Morphology and Structure

Since the gelation speed of sample BF/SAC-4 was too fast during the preparation process, which is unfavorable for industrial production, sample BF/SAC-3 was selected for heating treatments at 300 °C, 500 °C, and 700 °C for 24 h. The macroscopic and microscopic morphology after heating treatment is shown in Figure 7.

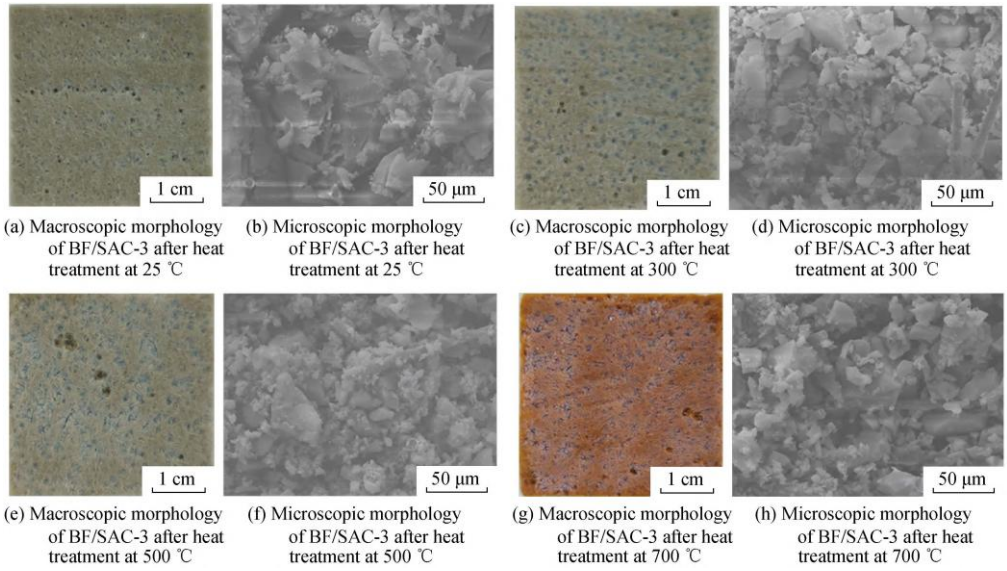

Figure 7 Surface morphology of sample BF/SAC-3 after heat treatment at different temperatures

As shown in Figure 7, heating treatment at 300 °C had no significant effect on sample BF/SAC-3. Heating at 500 °C caused the surface aerogel of sample BF/SAC-3 to shrink and crack [30], failing to maintain a complete blocky structure; the aerogel bulk partially fractured into granular particles. Influenced by the oxidation of Fe^{2+} in the basalt fibers to Fe^{3+} at high temperatures, sample BF/SAC-3 turned reddish-brown after 700 ° C treatment. Most of the aerogel matrix broke into small particles, making the sample more prone to dusting, but dimensional shrinkage remained minimal [31].

The pore structure of sample BF/SAC-3 after heat preservation for 24 h at different temperatures is shown in Figures 8 and 9. As shown in Figures 8 and 9, the isotherms of the heated sample BF/SAC-3 remain Type IV according to IUPAC classification, indicating that the sample retained abundant mesoporous structures. Moreover, the isotherm of the sample treated at 300 °C exhibited a distinct desorption platform, suggesting that the pore structure of the aerogel matrix became more regular during the heating process under the influence of surface energy. As organic groups in the sample (e.g., sizing agents on the fiber surface and hydrophobic modification groups on the aerogel surface) underwent oxidative decomposition around 300 °C, the specific surface area of BF/SAC-3 increased from 439.0 m^2/g to 581.5 m^2/g. However, changes in the pore shape led to a decrease in pore volume from 1.34 cm^3/g to 1.10 cm^3/g and a reduction in average pore size from 12.17 nm to 7.56 nm. After treatment at higher temperatures, the aerogel pore structure contracted further, with small pores fusing into fewer large ones, causing a continuous decrease in pore volume. However, the sample still retained part of the mesoporous structure even after 700 °C [32–33], indicating good structural stability.

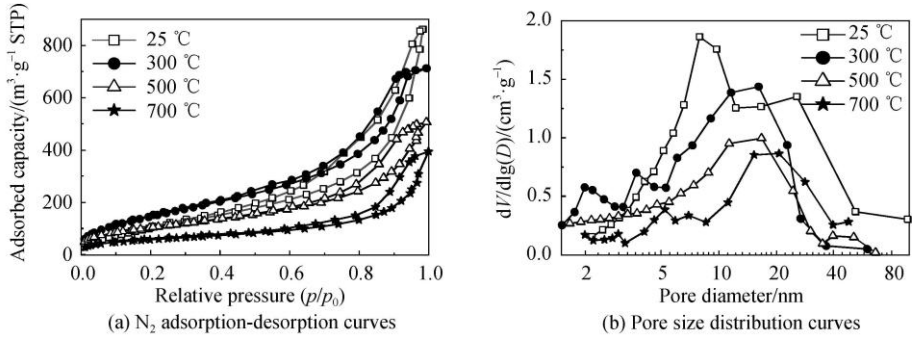

Figure 8 N2 adsorption and desorption curves and pore size distribution curves of sample BF/SAC-3 after heat treatment at different temperatures

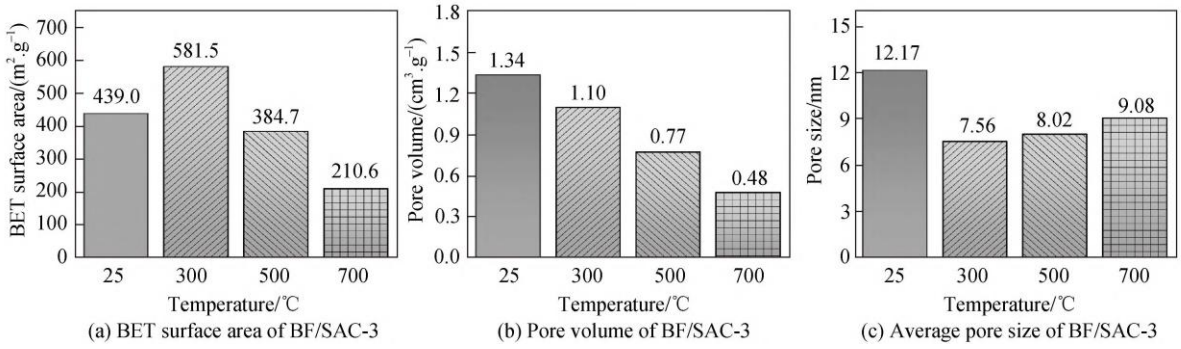

Figure 9 Pore parameters of sample BF/SAC-3 after heat treatment at different temperatures

Figure 10 shows the TG-DSC curves and FTIR spectra at different temperatures for sample BF/SAC-3. As shown in Figure 10a, the atmospheric pressure dried sample BF/SAC-3 possesses high thermal stability. Consistent with literature [34], the total mass loss at 1000 °C is 10%. However, within 300 °C, the mass loss of BF/SAC-3 is minor, at 1.6%; this stage primarily involves the desorption of adsorbed substances. At 321 °C, there is a mass loss step in the TGA curve of BF/SAC-3, and an exothermic peak appears in the DSC curve. At this temperature, organic components in BF/SAC-3—including sizing agents on the fiber surface and hydrophobic groups on the aerogel surface—undergo oxidative decomposition, causing a significant drop in sample mass [35]. This also verifies the reason for the increase in specific surface area of BF/SAC-3 after 300 °C treatment. Above 350 °C, the mass of BF/SAC-3 continues to decline, and the DSC curve generally exhibits endothermic characteristics; this stage mainly involves the decomposition of carbonates and further oxidation of organic residues. When the temperature exceeds 700 °C, the weight loss of BF/SAC-3 slows slightly. At this point, the oxidation of basalt fibers in BF/SAC-3 offsets some of the mass loss caused by carbide decomposition, and the color shifts from yellowish-brown to reddish-brown.

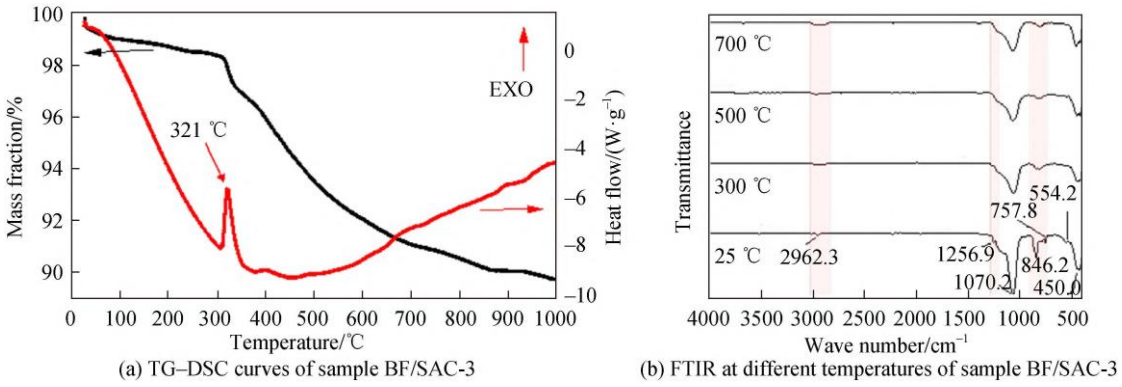

Figure 10 TG–DSC curves and FTIR at different temperatures of sample BF/SAC-3

As depicted in Figure 10b, the absorption band at 2962.3 cm^{-1} is assigned to asymmetric C–H stretching in Si–CH_3 moieties, while 1256.9 cm^{-1} corresponds to methyl deformation. The intense feature at 1070.2 cm^{-1} arises from asymmetric Si–O–Si stretching, with 846.2 cm^{-1} attributable to Si–CH_3 rocking. Bands at 757.8 cm^{-1} and 554.2 cm^{-1} represent symmetric Si–O–Si stretching and Si–O bending or SiO_2 lattice modes, respectively. The 450.0 cm^{-1} peak is associated with Si–O–Si skeletal deformation or low-frequency SiO_2 vibrations [36–37]. At room temperature, the atmospherically dried sample BF/SAC-3 shows high absorption peaks for Si–CH_3 and virtually no absorption peaks for Si–OH, indicating that hydroxyl groups on the sample surface have been largely replaced by methyl groups. The Si–CH_3 absorption band intensity progressively diminished with increasing thermal exposure, signifying oxidative degradation of surface-grafted hydrophobic methyl functionalities under elevated temperatures, corroborating thermogravimetric observations. Absorption peaks at other positions reflect the Si–O–Si skeletal structure of the aerogel in BF/SAC-3. After heating at 300 °C, the structure underwent certain changes; after higher temperature treatment, structural contraction occurred, and peak intensities decreased, consistent with BET test results.

3.2.2 High-Temperature Insulation and Mechanical Properties

Figure 11 shows the relationship between thermal conductivity and temperature for BF/SAC-3. Thermal conductivity exhibited linear temperature dependence yet remained remarkably suppressed at 0.0494 W/(m·K) under 500°C conditions, attesting to superior elevated-temperature insulating performance. Comparative thermal transport data for fiber-reinforced aerogel composites are presented in Table 2. BF/SAC-3 exhibits insulation performance comparable to composites relying on high-cost supercritical drying, confirming its stable and efficient insulation capability over a wide temperature range.

Table 2 Comparison of thermal conductivity of Fiber-reinforced aerogel composite

Source	Composite/ density/(g·cm⁻³)	Matrix phase	Enhanced phase	Thermal conductivity/ (W·m⁻¹·K⁻¹)	Drying method	Cost
[17]	0.27-0.39	Alumina-silica aerogel	4μm Mullite fiber 0.128 g/cm³	0.040-0.050 (500℃)	Supercritical drying	High
[34]	0.275-0.354	Al_2O_3-SiO_2 aerogels	Al_2O_3-SiO_2 fiber	0.0403-0.0545 (25℃)	Supercritical drying	High
[38]	0.1549-0.1612	Al_2O_3-SiO_2 aerogel	Aluminum silicate nanofibers	0.0262-0.264 (25℃)	Supercritical drying	High
[39]	—	SiO_2 aerogels	2.5-3.0μm Glass fiber	0.038 (25℃)	Freeze-drying	Low
[26]	—	SiO_2 aerogels	Glass fiber 100kg/m³	0.018 (25℃)	Supercritical drying	High
This work	0.159	SiO_2 aerogels	7μm basalt fiber 0.085 g/cm³	0.025 (25℃) 0.049 (500℃)	Atmospheric pressure drying	Low

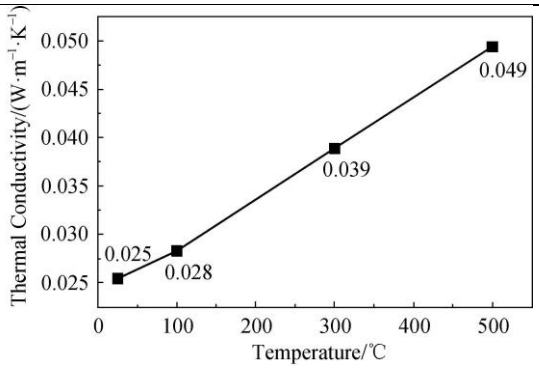

Figure 11 Thermal conductivity of sample BF/SAC-3 at different temperatures

Post-thermal conditioning compression behavior is illustrated in Figure 12. The stress-strain profiles preserved their triphasic deformation characteristics. Compressive stiffness initially rose with heating temperature before undergoing subsequent decline. Heat treatment homogenized the pore structure, reducing stress concentration during compression, increasing the modulus of BF/SAC-3 after 300°C treatment from 360.1 kPa to 1135.5 kPa, validating BET results. Compressive strength also improved significantly, from 121.0 kPa to 399.9 kPa. At 500°C, aerogel matrix cracking reduced the modulus to 544 kPa, but overall strength remained improved. After 700°C treatment, basalt fibers underwent phase transformation [40], drastically reducing structural strength; although the sample remained intact, mechanical properties dropped significantly (modulus 397 kPa, strength 289 kPa).

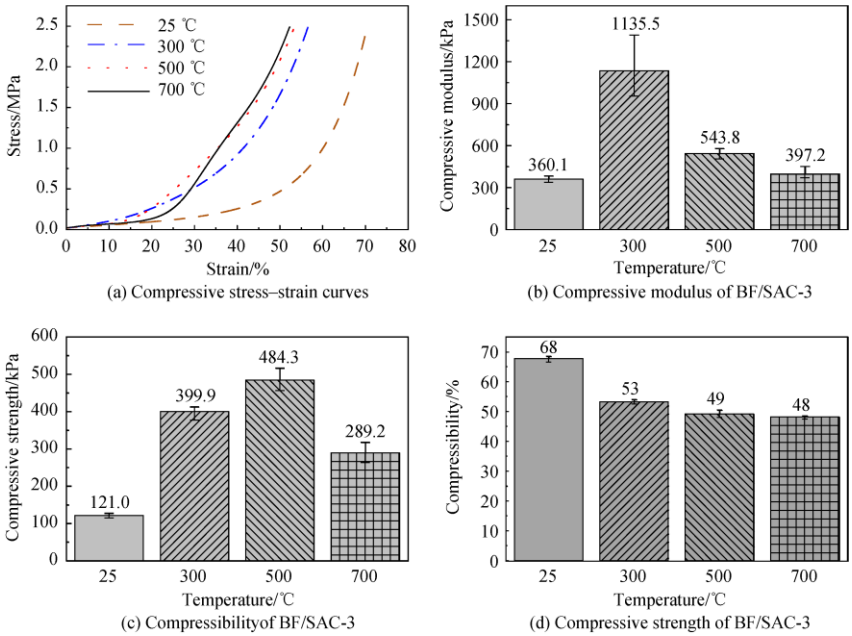

Figure 12 Compressive properties of sample BF/SAC-3 after heat treatment at different temperatures

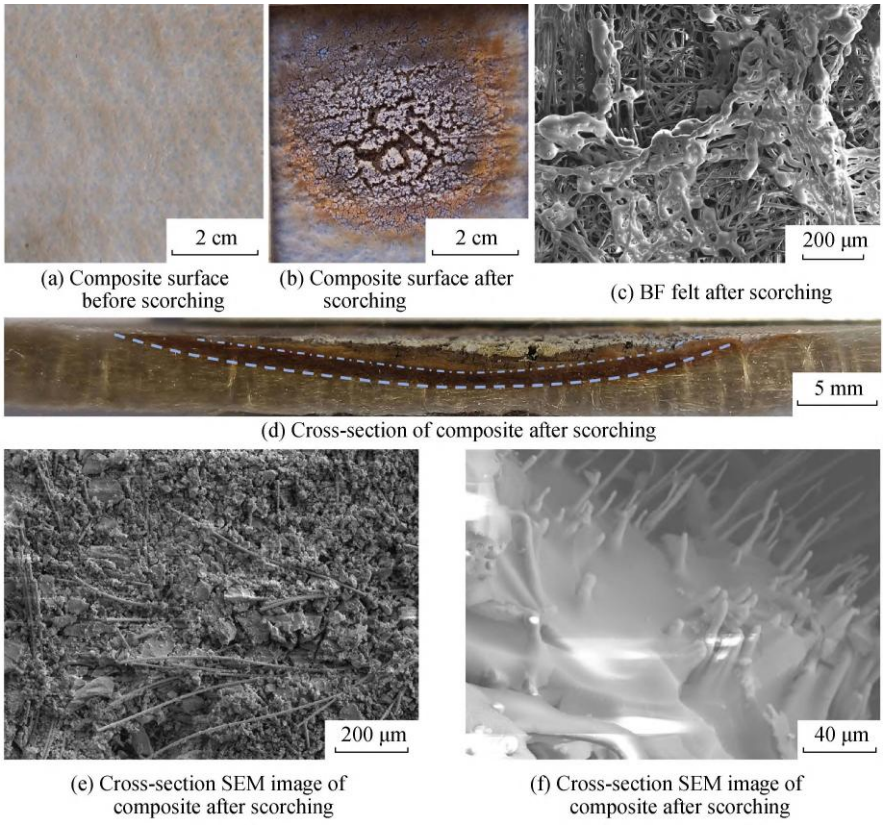

Figure 13 Morphology of sample BF/SAC-3 before and after flame exposure

Figure 13 shows the morphology of BF/SAC-3 before and after butane flame exposure. After 20 min of flame exposure, the surface cracked, and white particles sintered from SiO_2 aerogel appeared at the flame center. The heat-affected zone turned red-brown due to fiber oxidation, but the outermost region showed no significant change. As burning progressed, aerogel shrank into blocks covering lower fibers, and surface basalt fibers fused into a shell layer, inhibiting further flame damage. Benefiting from the high thermal stability of basalt fiber, although the surface layer weakened due to sintering, internal fibers remained intact. Severe sintering and shrinkage occurred only within a depth of about 2 mm (1/3 of the thickness) from the surface, while the middle layer changed color but retained structural integrity.

This study establishes a cost–performance–processability nexus for basalt fiber reinforced silica aerogel composites (BF/SAC) tailored to lithium-ion battery thermal runaway protection, resolving longstanding trade-offs between thermal insulation, mechanical robustness, and manufacturing scalability. By systematically tuning tetraethyl orthosilicate (TEOS) precursor concentration, the work identifies 1.00 mol/L as a critical formulation threshold that optimizes the silica sol–gel network while avoiding the overly rapid gelation observed at higher concentrations, which hinders industrial impregnation and mold filling. At this optimum, the composite achieves a low aerogel skeleton density of 0.08 g/cm³ and a mesoporous-dominated architecture (BET surface area: 439.0 m²/g), synergistically suppressing gaseous convection, solid conduction, and radiative heat transfer to deliver a room-temperature thermal conductivity of 0.0254 W/(m·K). This performance matches or exceeds that of glass fiber or aramid-reinforced aerogels produced via expensive supercritical drying, yet is realized here through an atmospheric pressure drying route that reduces equipment cost, operational hazard, and energy demand. Equally important, the basalt fiber needle-punched felt provides a three-dimensional load-bearing scaffold that compensates for the intrinsic brittleness of silica aerogels, yielding a compressive strength of 121 kPa and full elastic recovery—attributes essential for accommodating battery swelling, vibration, and assembly tolerances in electric vehicle packs. The successful substitution of low-cost basalt fiber for high-performance ceramic fibers (e.g., mullite, SiC) without sacrificing high-temperature stability marks a pivotal advance in materials selection, aligning with the economic constraints of automotive mass production.

High-temperature evaluations further demonstrate that BF/SAC-3 retains functional integrity under conditions mimicking severe battery thermal runaway. After 24 h at 500 °C, the composite sustains a thermal conductivity of only 0.0494 W/(m·K), outperforming many commercial insulation felts, while compressive strength nearly quadruples due to pore-structure homogenization and partial sintering-induced stiffening. Even at 700 °C—approaching the surface temperature of runaway ternary lithium batteries—the basalt fiber skeleton prevents catastrophic disintegration, maintaining structural continuity despite aerogel granulation and a modest 10% total mass loss. Extreme flame exposure (1090 °C butane flame, 20 min) confirms the formation of a self-limiting protective layer: surface sintering of silica aerogel and partial vitrification of basalt fibers create a dense, thermally resistive crust that confines damage to a shallow ~2 mm depth, leaving the interior intact and thermally insulative. These findings highlight a crucial safety feature—progressive rather than abrupt failure—which is indispensable for passive thermal barriers. While organic hydrophobic groups decompose above 300 °C, the inorganic Si–O–Si backbone remains stable to 1000 °C, and mesoporosity is largely preserved, ensuring continued insulation. Future work should focus on hybridizing the aerogel matrix with infrared opacifiers (e.g., TiO_2, SiC nanoparticles) to further suppress radiative heat transfer at >600 ° C, and on scaling the atmospheric drying process to continuous roll-to-roll production. Overall, this work delivers a commercially viable, high-performance thermal protection pad that reconciles ultra-low thermal conductivity, mechanical compliance, extreme heat resistance, and low manufacturing cost—directly addressing a key safety bottleneck in new energy vehicles.

4. Conclusion

This work successfully prepared basalt fiber needle-punched felt reinforced silica aerogel composites via an atmospheric pressure drying process and systematically studied their thermal protection and mechanical properties. The main conclusions are as follows: TEOS concentration significantly affected structural integrity. At 1.00 mol/L, the aerogel matrix density was as low as 0.08 g/cm³ with minimal shrinkage (33.3%), forming a continuous mesoporous structure (specific surface area 439.0 m²/g). This endowed the material with excellent insulation performance (room-temperature thermal conductivity 0.0254 W/(m·K), cold-side temperature of 106°C under a 600°C hot surface) and mechanical properties (compression modulus 360 kPa, compression strength 121 kPa). The material maintained functional stability under high-temperature environments. After 500°C treatment, thermal conductivity was only 0.0494 W/(m·K), and compressive strength increased to 484 kPa due to pore structure homogenization. At 700°C, although aerogel granulation occurred, the basalt fiber skeleton maintained structural integrity, with a mass loss rate of only 10% at 1000°C. Butane flame exposure for 20 min verified excellent flame resistance. A mixed sintering protective layer of aerogel and fiber formed on the surface, effectively blocking heat penetration. The sample did not burn through, with sintering confined to a shallow depth of about 2 mm, while the internal structure remained intact.

References

[1] FENG X N, OUYANG M G, LIU X, et al. Thermal runaway mechanism of lithium ion battery for electric vehicles: A review[J]. Energy Storage Mater, 2018, 10: 246-267.

[2] SUN T, YAN Y L, WANG X H, et al. A comprehensive study on heat transfer mechanism and thermal runaway suppression of the lithium-ion battery[J]. Int J Heat Mass Transf, 2021, 245: 127027.

[3] JIAN Y, JIANG Y G, FENG J Z, et al. Preparation, properties, and applications of waterproof high-temperature insulation materials[J]. J Chin Ceram Soc, 2021, 53(3): 718-732.

[4] SHI X J, ZHANG R F, HE S, et al. Preparation and thermal insulation properties of glass fiber toughened SiO_2 aerogel composites[J]. J Chin Ceram Soc, 2016, 44(1): 129-135.

[5] ZOU K Y, XU J, ZHAO M K, et al. Effects and mechanism of thermal insulation materials on thermal runaway propagation in large-format pouch lithium-ion batteries[J]. Process Saf Environ Prot, 2020, 185: 1352-1361.

[6] S S S, RAI N, CHAUHAN I. Multifunctional Aerogels: A comprehensive review on types, synthesis and applications of aerogels[J]. J Sol Gel Sci Technol, 2020, 105(2): 324-336.

[7] AKHTER F, SOOMRO S A, INGLEZAKIS V J. Silica aerogels; a review of synthesis, applications and fabrication of hybrid composites[J]. J Porous Mater, 2021, 28(5): 1387-1400.

[8] BARRIOS E, FOX D, LI SIP Y Y, et al. Nanomaterials in advanced, high-performance aerogel composites: A review[J]. Polymers, 2019, 11(4): 726.

[9] NI Y Y, ZHU J Y, GAO Y, et al. Preparation of silica aerogels based on ternary phase transition control[J]. J

Chin Ceram Soc, 2021, 52(8): 2685-2694.
[10] ZHANG X S, JIANG Y G, XUN N, et al. Thermal stable, fire-resistant and high strength SiBNO fiber/SiO_2 aerogel composites with excellent thermal insulation and wave-transparent performances[J]. Mater Today Commun, 2022, 33: 104261.
[11] FENG J B, MA Z W, WU J P, et al. Fire-safe aerogels and foams for thermal insulation: From materials to properties[J]. Adv Mater, 2021, 37(3): 2411856.
[12] SHARMA J, SHUKLA S, SINGH O, et al. Multi-field and multi-scale characterization of non-supercritical dried silica aerogel-based glass blankets: Investigating thermal, mechanical, acoustic, and fire performance[J]. J Sol Gel Sci Technol, 2020, 108(1): 60-72.
[13] GUO J Y, CHEN Z W, SU L J, et al. Effect of radiation heat transfer on thermal insulation performance of silica aerogel composites[J]. J Chin Ceram Soc, 2021, 51(7): 1811-1818.
[14] HEYER M, BERKEFELD A, VOEPEL P, et al. Advanced opacified fiber-reinforced silica-based aerogel composites for superinsulation of exhaust tubing systems in semi-stationary motors[J]. Materials, 2020, 13(12): 2677.
[15] HEYER M, ESSER B, GUELHAN A, et al. Mixed oxide aerogels with high-performance insulating properties for high-temperature space application[J]. Adv Eng Mater, 2021, 25(21): 2300625.
[16] XUE J Y, HAN R N, LI Y M, et al. Advances in multiple reinforcement strategies and applications for silica aerogel[J]. J Mater Sci, 2020, 58(36): 14255-14283.
[17] PENG F, JIANG Y G, FENG J, et al. Thermally insulating, fiber-reinforced alumina-silica aerogel composites with ultra-low shrinkage up to 1500°C[J]. Chem Eng J, 2021, 411: 128402.
[18] LI Z, CHENG X D, HE S, et al. Aramid fibers reinforced silica aerogel composites with low thermal conductivity and improved mechanical performance[J]. Compos Part A Appl Sci Manuf, 2016, 84: 316-325.
[19] WU Q, YANG M M, CHEN Z F, et al. A layered aerogel composite with silica fibers, SiC nanowires, and silica aerogels ternary networks for thermal insulation at high-temperature[J]. J Mater Sci Technol, 2021, 204: 71-80.
[20] KIM S H, LEE J H, KIM J W, et al. Interfacial behaviors of basalt fiber-reinforced polymeric composites: A short review[J]. Adv Fiber Mater, 2020, 4(6): 1414-1433.
[21] GE S K, NI Y, ZHOU F B, et al. A passive fire protection method for main cables and slings of suspension bridges utilizing fiber felt/aerogel composites[J]. Constr Build Mater, 2021, 408: 133822.
[22] YUE X, CHEN J Y, LI H X, et al. Research progress on structural reinforcement of aerogel materials[J]. J Chin Ceram Soc, 2021, 49(4): 681-691.
[23] GONTHIER J, SCOPPOLA E, RILLING T, et al. Solvent cavitation during ambient pressure drying of silica aerogels[J]. Langmuir, 2020, 40(25): 12925-12938.
[24] SIVARAMAN D, ZHAO S Y, ISWAR S, et al. Aerogel spring-back correlates with strain recovery: Effect of silica concentration and aging[J]. Adv Eng Mater, 2021, 23(10): 2100376.
[25] WANG S, SU X L, ZHENG W J, et al. Study on preparation of SiO_2/PTFE aerogel-like materials via atmospheric drying and their thermal insulation performance[J]. J Sol Gel Sci Technol, 2019, 109(1): 204-214.
[26] SHAN J Q, SHAN Y P, ZOU C, et al. Cost-effective preparation of hydrophobic and thermal-insulating silica aerogels[J]. Nanomaterials, 2014, 14(1): 119.
[27] XU Y Y, ZHANG H, HE L J, et al. Regulating the concentration of silica Sol to prepare high thermal insulation ceramic nanofiber aerogel composites[J]. J Phys: Conf Ser, 2017, 2789(1): 012003.
[28] ZHOU L, WU L, WU T, et al. A 'ceramer' aerogel with unique bicontinuous inorgani-organic structure enabling super-resilience, hydrophobicity, and thermal insulation[J]. Mater Today Nano, 2020, 22: 100306.
[29] BUSCARINO G, ARDIZZONE V, VACCARO G, et al. Sintering process of amorphous SiO_2 nanoparticles investigated by AFM, IR and Raman techniques[J]. J Non Cryst Solids, 2011, 357(8-9): 1866-1870.
[30] KANG D W, JIA S D, ZHAO C H, et al. High-temperature resistance performance of silica aerogel composites through fiber reinforcement[J]. Ceram Int, 2019, 50(15): 26829-26838.
[31] ZHAO W P, JI Y C, PANG Y F, et al. Preparation of Al_2O_3-SiO_2 aerogel by ambient pressure drying for thermal insulation application[J]. J Porous Mater, 2021, 30(5): 1753-1761.
[32] SUN D, LI K, SUI X Y, et al. Research of silica aerogels prepared by acidic silica Sol under the condition of atmospheric pressure drying[J]. J Porous Mater, 2018, 25(2): 341-349.
[33] LI Z, DENG Y M, WANG Y, et al. Preparation of hydrophobic SiO_2 aerogel with high thermal stability by argon heat treatment[J]. J Chin Ceram Soc, 2020, 50(5): 1325-1334.
[34] YU Y X, PENG K H, FANG J Y, et al. Mechanical and thermal conductive properties of fiber-reinforced silica-alumina aerogels[J]. Int J Appl Ceram Technol, 2018, 15(5): 1138-1145.

[35] CAI H F, JIANG Y G, FENG J, et al. Preparation of silica aerogels with high temperature resistance and low thermal conductivity by monodispersed silica Sol[J]. Mater Des, 2020, 191: 108640.
[36] GUO J J, LUO K Q, ZOU W Q, et al. Enhancing mesopore volume and thermal insulation of silica aerogel via ambient pressure drying-assisted foaming method[J]. Materials, 2020, 17(11): 2641.
[37] DUAN Y D, WANG L J, LI S Y, et al. Modulating pore microstructure of silica aerogels dried at ambient pressure by adding N-hexane to the solvent[J]. J Non Cryst Solids, 2019, 610: 122312.
[38] HAO M Y, CHEN H L, XIA C K, et al. Al_2O_3-SiO_2 aerogel reinforced with aluminum silicate nanofibers: A strategy to preserve the properties of Al_2O_3-SiO_2 aerogel[J]. J Sol Gel Sci Technol, 2019, 109(2): 523-533.
[39] XUE J Y, LIU L P, MENG Y L, et al. Constructing powerful interface between glass fiber and silica aerogel via an interfacial molecular bridge allows for excellent acoustic-thermal insulation composites[J]. Constr Build Mater, 2020, 465: 140260.
[40] SARASINI F, TIRILLO J, SEGHINI M C. Influence of thermal conditioning on tensile behaviour of single basalt fibres[J]. Compos Part B Eng, 2018, 132: 77-86.